SLAC-PUB-14976

Prepared for submission to JCAP

Limits on Large Extra Dimensions Based on Observations of Neutron Stars with the Fermi-LAT

Fermi-LAT Collaboration

M. Ajello[a] L. Baldini[b] G. Barbiellini[c] D. Bastieri[d] K. Bechtol[a] R. Bellazzini[b] B. Berenji[a] E.D. Bloom[a] E. Bonamente[e] A.W. Borgland[a] J. Bregeon[b] M. Brigida[f] P. Bruel[g] R. Buehler[a] S. Buson[d] G.A. Caliandro[h] R.A. Cameron[a] P.A. Caraveo[i] J.M. Casandjian[j] C. Cecchi[e] E. Charles[a] A. Chekhtman[k] J. Chiang[a] S. Ciprini[l] R. Claus[a] J. Cohen-Tanugi[m] J. Conrad[n] S. Cutini[l] A. de Angelis[o] F. de Palma[f] C.D. Dermer[p] E. do Couto e Silva[a] P.S. Drell[a] A. Drlica-Wagner[a] T. Enoto[a] C. Favuzzi[f] S.J. Fegan[g] E.C. Ferrara[q] Y. Fukazawa[r] P. Fusco[f] F. Gargano[s] D. Gasparrini[l] S. Germani[e] N. Giglietto[f] F. Giordano[f] M. Giroletti[t] T. Glanzman[a] G. Godfrey[a] P. Graham[a] I.A. Grenier[l] S. Guiriec[u] M. Gustafsson[d] D. Hadasch[k] M. Hayashida[a] R.E. Hughes[v] A.S. Johnson[a] T. Kamae[a] H. Katagiri[w] J. Kataoka[x] J. Knödlseder[y] M. Kuss[b] J. Lande[a] L. Latronico[b] A.M. Lionetto[z] F. Longo[c] F. Loparco[f] M.N. Lovellette[p] P. Lubrano[e] M.N. Mazziotta[s] P.F. Michelson[a] W. Mitthumsiri[a] T. Mizuno[r] C. Monte[f] M.E. Monzani[a] A. Morselli[z] I.V. Moskalenko[a] S. Murgia[a] J.P. Norris[z] E. Nuss[m] T. Ohsugi[r] A. Okumura[a] E. Orlando[a] J.F. Ormes[aa] M. Ozaki[ab] D. Paneque[ac] M. Pesce-Rollins[b] M. Pierbattista[m] F. Piron[m] G. Pivato[ad] S. Rainò[f] M. Razzano[b] S. Ritz[ae] M. Roth[af] P.M. Saz Parkinson[ae] J.D. Scargle[ah] T.L. Schalk[ai] C. Sgrò[b] E.J. Siskind[aj] G. Spandre[b] P. Spinelli[f] D.J. Suson[ak] H. Tajima[a] H. Takahashi[al] T. Tanaka[a] J.G. Thayer[a] J.B. Thayer[a] L. Tibaldo[d] M. Tinivella[b] D.F. Torres[h] E. Troja[q] Y. Uchiyama[a] T.L. Usher[a] J. Vandenbroucke[a] V. Vasileiou[m] G. Vianello[a] V. Vitale[z] A.P. Waite[a] B.L. Winer[v] K.S. Wood[p] M. Wood[a] Z. Yang[n] S. Zimmer[n]

[a]Stanford University, Applied Physics Department, Physics Department, SLAC National Accelerator Laboratory, W. W. Hansen Experimental Physics Laboratory

[b]INFN and University of Pisa

Work supported in part by US Department of Energy contract DE-AC02-76SF00515.

SLAC National Accelerator Laboratory, Menlo Park, CA 94025

[c]INFN Trieste
[d]INFN Padova
[e]INFN Perugia
[f]Dipartimento Interateneo di Fisica dell'Università e Politecnico di Bari and INFN Sezione di Bari
[g]Laboratoire Leprince-Ringuet, École polytechnique
[h]Institut de Ciències de l'Espai
[i]INAF-IASF, Milano
[j]Laboratoire AIM, Saclay
[k]Artep, Inc.
[l]ASI Science Data Center
[m]Laboratoire Univers et Particules de Montpellier
[n]Stockholms Universitet
[o]INFN and University of Udine
[p]Naval Research Laboratory, Space Science Division
[q]NASA Goddard Space Flight Center
[r]Hiroshima University, Physical Sciences Department
[s]INFN Sezione di Bari
[t]INAF Istituto di Radioastronomia, Bologna
[u]University of Alabama in Huntsville
[v]The Ohio State University
[w]Ibaraki University
[x]Waseda University
[y]IRAP CNRS
[z]INFN Roma Tor Vergata
[h]INFN Perugia
[z]Boise State University
[aa]University of Denver
[ab]Institute of Space and Aeronautical Science (JAXA)
[ac]Max-Planck-Institut für Physik, München
[ad]University of Padova, Fisica
[ae]University of California, Santa Cruz Institute for Particle Physics
[af]University of Washington
[ah]NASA Ames Research Center
[b]INFN and University of Pisa
[aj]NYCB Real-Time Computing Inc.
[ak]Purdue University - Calumet
[al]Hiroshima University, Astrophysical Science Center

E-mail: bijanb@alumni.stanford.edu, elliott@slac.stanford.edu, johann.cohen-tanugi@lupm.in2p3.fr

Abstract. We present limits for the compactification scale in the theory of Large Extra Dimensions (LED) proposed by Arkani-Hamed, Dimopoulos, and Dvali. We use 11 months of data from the Fermi Large Area Telescope (Fermi-LAT) to set gamma ray flux limits for 6 gamma-ray faint neutron stars (NS). To set limits on LED we use the model of Hannestad and Raffelt (HR) that calculates the Kaluza-Klein (KK) graviton production in supernova cores and the large fraction subsequently gravitationally bound around the resulting NS. The predicted decay of the bound KK gravitons to $\gamma\gamma$ should contribute to the flux from NSs. Considering 2 to 7 extra dimensions of the same size in the context of the HR model, we use Monte Carlo techniques to calculate the expected differential flux of gamma-rays arising from these KK gravitons, including the effects of the age of the NS, graviton orbit, and absorption of gamma-rays in the magnetosphere of the NS. We compare our Monte Carlo-based differential flux to the experimental differential flux using maximum likelihood techniques to obtain

our limits on LED. Our limits are more restrictive than past EGRET-based optimistic limits that do not include these important corrections. Additionally, our limits are more stringent than LHC based limits for 3 or fewer LED, and comparable for 4 LED. We conclude that if the effective Planck scale is around a TeV, then for 2 or 3 LED the compactification topology must be more complicated than a torus.

Contents

1 Introduction

In the Standard Model of particle physics, gravity is not unified with the other 3 fundamental forces .This is manifested by the *hierarchy problem*, the fact that the electroweak mass scale $M_{\rm EW} \sim 1\,{\rm TeV}$ is many orders of magnitude smaller than the Planck mass scale $M_{\rm P} \approx 1.22 \times 10^{16}\,{\rm TeV}$ [1]. Arkani-Hamed, Dimopoulos, and Dvali (ADD) propose a model of Large Extra Dimensions (LED) as a solution for the hierarchy problem. The ADD scenario may be embedded into string theory, which allows for the existence of compactified extra dimensions. Due to the presence of n extra dimensions, at length scales smaller than the size of the extra dimensions, the gravitational potential between test masses has a $1/r^{n+1}$ dependence; however, on scales larger than the size of the extra dimensions the gravitational potential reverts to the ordinary $1/r$ dependence. For a given n, if all the extra dimensions are toroidally compactified, *i.e.*, have the same size R, the effective Planck mass in the $(n+4)-$dimensional space, M_D, is related to the reduced Planck mass $\bar{M}_P = M_P/\sqrt{8\pi}$ by the relation:

$$\bar{M}_P^2 = R^n M_D^{n+2}. \tag{1.1}$$

In the ADD model, the hierarchy problem is solved because the presence of LED brings the effective Planck mass, M_D, to the TeV scale, the truly fundamental scale of gravity. As a consequence, the associated Kaluza-Klein gravitons, denoted by G_{KK}, are massless in the bulk, but they have mass on the 3-brane related to their momentum in the bulk (unlike the gravitons of General Relativity).

According to the ADD model, it is possible to place constraints on extra dimensions by G_{KK} emission from nucleon-nucleon gravibremsstrahlung in type II supernova cores, $NN \rightarrow NNG_{KK}$. ADD obtain limits from Supernova (SN) 1987A, assuming pion-exchange mediated by the strong force as the dominant process. Hanhart, Reddy and Savage (2001) assume a different process[2]. They use nucleon-nucleon gravibremsstrahlung mediated by nucleon-nucleon scattering to obtain the

specification	Fermi-LAT	EGRET
68% containment PSF (°) at 200 MeV	2.8	3.3
Effective Area (cm^2) at 200 MeV	3000	1000
Energy Resolution (%) at 200 MeV	13	9.3
flux sensitivity ($cm^{-2}s^{-1}$)	6×10^{-9}	1.3×10^{-7}

Table 1: Comparison of performance specifications of Fermi-LAT and EGRET, as relevant for the gamma-ray energies considered in this paper[5, 6]. Flux sensitivity is evaluated for a high-latitude point source with a E^{-2} spectrum, with 1 year of data, for $E > 100$ MeV. EGRET effective area is quoted for Class A events.

emission rate for KK gravitons. Furthermore, they indicate that the actual details of the scattering process are not important in the soft-radiation limit, where the energy of the outgoing gravitons is much less than the energy other incoming nucleons[2]. Then they proceed to obtain limits for $n = 2$ and $n = 3$ extra dimensions from SN1987A. This is based on the argument that the observed neutrino luminosity sets an upper bound of 10^{19} ergs $g^{-1}s^{-1}$ on the energy loss rate into particles other than neutrinos such as G_{KK}[3].

Hannestad and Raffelt (henceforth HR [4]) extend this idea to neutron stars, proposing that if the KK gravitons are bound in the gravitational potential of a proto-neutron star as it evolves into a neutron star, then the flux of photons from KK graviton decays, $G_{KK} \rightarrow 2\gamma$, could be used to set a limit on extra dimensions. They use EGRET results to set limits on LED. However, they do not place direct flux limits on the neutron stars not detected by EGRET. Rather, they quote their flux upper limit as the 1 yr point-source sensitivity of EGRET for a high latitude point source with a E^{-2} spectrum (see section 2.1), and derive limits on LED more restrictive than from arguments based on KK graviton emissivities from SN 1987A. To obtain upper limits, we follow similar theoretical arguments as HR, but we perform a very different analysis, including spectral corrections and upper limit spectral analysis with Fermi-LAT data, on 6 gamma-ray faint NS.

2 Data Analysis

2.1 Experimental Methods

The Fermi-LAT is a gamma-ray imaging pair-conversion telescope, consisting of an anti-coincidence detector, tracker, calorimeter, and electronics modules. The details of the Fermi-LAT are discussed by Atwood *et al.*[5]. The Fermi-LAT features improved performance compared to its predecessor γ-ray observatory, EGRET. Some of these specifications, relevant to this study, are compared in Table 1.

Setting flux limits on sources requires knowledge of background point sources and diffuse emission. We make use of the publicly available diffuse models developed by the Fermi-LAT collaboration: the Galactic diffuse emission model, *gll_iem_v02.fit*[7, 8]; and the isotropic model, *isotropic_iem_v02.txt*[9]. The Galactic diffuse model is allowed to vary in a region of interest (ROI) around each source by multiplying by a power-law spectral function, as described in [10], effectively making the spectrum harder or softer. The scale for the power-law is 100 MeV, and the index is allowed to vary between -0.1 and 0.1 (a value of 0 implies no correction to the model). The background point sources are modeled by fixing the spectral parameters from the first year Fermi-LAT (1FGL) catalog [10].

The data sample consists of a selection of 11 months of all-sky data obtained with the Fermi-LAT instrument, using a time interval beginning with the start of survey mode, August 4, 2008, until July 4, 2009. This time interval is chosen to be consistent with the 1FGL catalog, so that nearby point sources detected with high significance may be modeled appropriately as power-law sources [10]. The instrument response function (IRF) chosen is *P6_V3_DIFFUSE*[11], as is the case for the 1FGL catalog. This IRF specifies a parametrization of effective area, energy resolution, and point spread function. We select data from the 1FGL catalog dataset for regions of interest (ROIs) corresponding to each source described further in this paper. This dataset excludes events for which the rocking

source name	RA (°)	Dec. (°)	ℓ (°)	b (°)	P (s)	d (kpc)	Age (Myr)	$B_{\rm surf}$ (G)
RX J1856−3754	284.15	−37.90	358.61	−17.21	7.05	0.16	3.76	1.47×10^{13}
J0108−1431	17.04	−14.35	140.93	−76.82	0.808	0.24	166	2.52×10^{11}
J0953+0755	148.29	7.93	228.91	43.7	0.25	0.26	17.5	2.44×10^{11}
J0630−2834	97.71	−28.58	236.95	−16.76	1.24	0.33	2.77	3.01×10^{12}
J1136+1551	174.01	15.85	241.90	69.20	1.19	0.36	5.04	2.13×10^{12}
J0826+2637	126.71	26.62	196.96	31.74	0.53	0.36	4.92	9.64×10^{11}

Table 2: Astrophysical properties of neutron star sources analyzed in this work, with sources in increasing order of distance. Coordinates, periods. distances, ages, and surface magnetic field strengths are obtained from the ATNF Catalog [12].

angle is larger than 43°, because of contamination from the Earth's limb due to interactions of cosmic rays with Earth's upper atmosphere. For the same reason, for each ROI, events for which the zenith angle is larger than 105° are excluded. There is also a good time interval (GTI) cut applied, as described in Ref. [10].

2.2 Selection of Neutron Stars

A query is made on the Australia Telescope National Facility (ATNF) radio pulsar catalog to select NS [12]. In order to obtain the best limits, we reject candidate sources that have associations with γ-ray sources detected in the 1FGL catalog. To minimize attenuation of the putative KK graviton decay signal, as discussed in section IV, we choose NS that satisfy the following criteria: distance $d < 0.40$ kpc; surface magnetic field $B_{\rm surf} < 5 \times 10^{13}$ G; and characteristic age $t_{\rm age} < 2 \times 10^{8}$ yr. We take the NS ages as the spin-down ages of the pulsars, for consistency over all sources; the corrected ages may differ, as discussed in Ref. [13]. However, consideration of the corrected ages hardly affects the limits presented here. In addition, the γ-ray sky as viewed by Fermi-LAT is filled with sources near the Galactic plane, and diffuse components are also dominant and have large systematic uncertainties at low latitudes; we require for Galactic latitude (b), that $|b| > 15°$ for candidate neutron stars. Applying all the above selection criteria to the ATNF catalog, 6 sources remain for analysis, with parameters as shown in Table 2.

2.3 Gamma-ray Spectral Limits

Fermi-LAT gamma-ray events are selected in a 12° radius ROI centered on each NS source listed in Table 2. Given the limitations of the dataset we use and the expected spectral energy distribution from gamma rays from trapped KK graviton decay, only gamma-ray events with energies in the range 100 MeV to 400 MeV are considered. Although desirable, going below 100 MeV is not feasible for this analysis using *P6_V3_DIFFUSE*. Before obtaining upper limits for each source, a model for the corresponding ROI is developed, inclusive of 1FGL sources and the 2 components of diffuse emission (no putative neutron star source is included in this step). 1FGL catalog sources within a 14° radius are parametrized as point sources with a power-law spectral energy distribution, with fluxes and spectral indices *fixed* at catalog values; those sources farther than 14° away are not considered. These parameters are fixed due to the small gamma-ray energy range (100 MeV-400 MeV) that we use, which leaves little spectral range to perform accurate fitting. An initial unbinned likelihood fit is done in order to determine *only* the diffuse parameters. For the isotropic diffuse component, the parameter to be determined is normalization, while for the Galactic diffuse component, we consider the normalization and the spectral index. The analysis, including the diffuse fitting and upper limit determination, is performed with the Fermi *ScienceTools* program `pyLikelihood`, featuring maximum likelihood-based fitting. Version *09-17-00* of the Fermi-LAT *ScienceTools* is used[14]. For the neutron star RX J1856−3754, a counts map of 100-400 MeV photons in a $10° \times 10°$ region, convolved with a Gaussian approximation to the Fermi-LAT PSF, is shown in the left panel of Figure 1. The residual counts map (determined from comparison of the counts map to the model-based map), for source RX J1856−3754, is displayed in the right panel of Figure 1. Figure 2 shows a residual counts plot

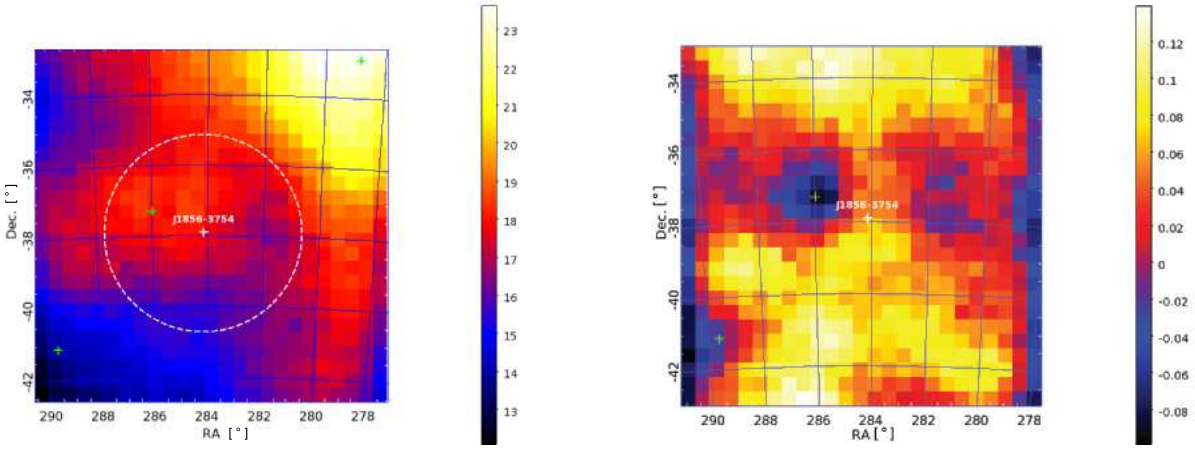

Figure 1: Left: Counts map from data, for source RX J1856−3754, convolved with a Gaussian approximation to the Fermi-LAT PSF, in order to reduce statistical fluctuations without dramatically reducing the angular resolution. The colorbar shows counts per pixel. The white dashed circle shows the 200 MeV PSF. Right: Residual map, (counts-model)/model, for the same source, based on the 1FGL model with the fitted diffuse model. The pixel size is 0.4° for both. Green crosses show 1FGL point sources, and the putative γ-ray source is at the center.

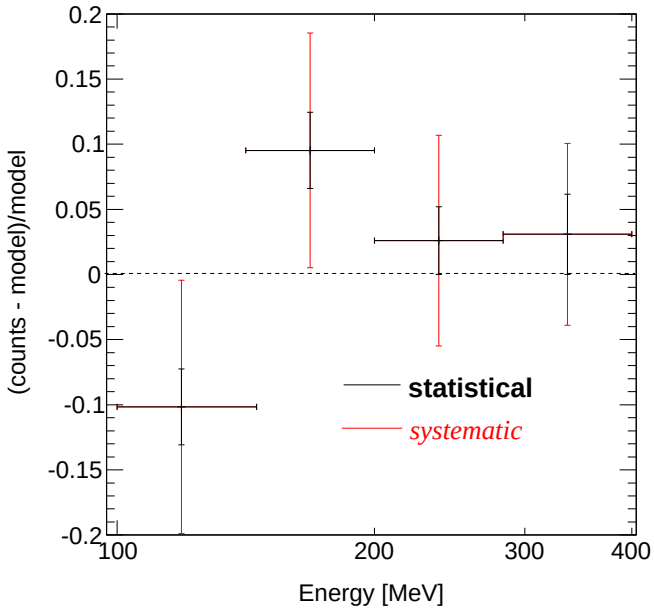

Figure 2: Residual plot of counts over the 10° square region around source RX J1856−3754. Black horizontal bands indicate the energy range for each point, and black vertical bands represent statistical uncertainties, while red vertical bands represent systematic uncertainties of about 10% at 100 MeV, and decreasing to 5% at 562 MeV[15].

versus energy, obtained by integrating over the counts map spatial dependence, and subtracting the data counts from model counts and dividing by the model counts.

A spectral model, which determines the differential flux $d\Phi/dE$, for each source and number of

extra dimensions n, is developed in the next section. A significant difference in the data analysis technique from Hannestad and Raffelt lies in considering the differential flux rather than the integral flux, in determining limits on R; this is a more accurate and optimal method in setting limits in a Fermi-LAT analysis, when comparing the data to a pre-defined theoretical distribution. Complete details of the theoretical development of the differential flux, as well as analysis methods, can be found in [13].

3 Calculating the Spectral Model for KK Graviton Decay $\gamma-$Rays from NS

In the following subsections, we explain how we calculate the gamma-ray spectrum. Important departures from the analysis of HR in forming the theoretical differential flux, $d\Phi/dE$, to be compared to Fermi-LAT observations include: attenuation of the signal due to the age of the neutron star, orbital position and velocity of the G_{KK}, decay of $G_{KK} \to 2\gamma$, and attenuation of the signal due to magnetic field (which is position and velocity dependent). These features are included via a Monte Carlo simulation of about 10^7 G_{KK} in orbit for each NS source and for $n = 2, 3, \ldots, 7$ extra dimensions.

3.1 Theoretical Model

Following HR, we start with the differential distribution of G_{KK} created during the proto-neutron star core collapse with total energy ω and mass m:

$$\frac{\mathrm{d}^2 N_{\mathrm{KK,n}}}{\mathrm{d}\omega \mathrm{d}\mu} = \frac{\mathrm{d}^2 Q_n}{\omega \mathrm{d}\omega \mathrm{d}\mu} \Delta t_{NS} V_{NS} \ . \tag{3.1}$$

We will make use of notations defined in HR, that we rewrite here for completeness: Q_n is the total energy loss rate per unit volume into KK gravitons which depends on n; $\mu = m/\omega$ is the inverse of the initial Lorentz factor of the G_{KK}; $\Delta t_{NS} \simeq 7.5$ s is the time-scale for emission of G_{KK} during the core collapse; and $V_{NS} = \frac{4}{3}\pi R_{NS}^3$ is the volume of the proto-neutron star (and current neutron star) of radius $R_{NS} \simeq 13$ km. According to HR, we have:

$$\frac{\mathrm{d}^2 Q_n}{\mathrm{d}\omega \mathrm{d}\mu} = Q_0 (RT)^n \Omega_n G_{n-1}(\mu) F_n \left(\frac{\omega}{T}\right) \ , \tag{3.2}$$

where R is the extra dimension size, as in eq. (1), $T \gtrsim 30$ MeV is the supernova core temperature (see Section 5), and $\Omega_n = 2\pi^{n/2}/\Gamma(n/2)$ is the surface of the n-dimensional unit hypersphere, with $\Gamma(...)$ as the Gamma function. We also have,

$$Q_0 = \frac{512}{5\pi^{3/2}} \frac{G_N \sigma n_B^2 T^{7/2}}{M^{1/2}} \tag{3.3}$$

$$= 1.100 \times 10^{22} \mathrm{MeV\ cm^{-3} s^{-1}} \left(T/30\ \mathrm{MeV}\right)^{7/2} \left(\rho/3 \times 10^{14}\ \mathrm{g\ cm^{-3}}\right)^2 \left(f_{KK}/0.0075\right) , \tag{3.4}$$

where Newton's constant is $G_N = 6.708 \times 10^{-33} \hbar c\, (\mathrm{MeV}/c^2)^{-2}$, σ is the nucleon-nucleon scattering cross section of 25 mb, n_B is the number density of baryons of 0.16 fm^{-3}, and M is the isospin-averaged nucleon mass of 938 MeV/c^2. $f_{KK} \simeq 0.01$ is the estimated fraction of core-collapse energy radiated away as G_{KK} [16, 17]. In eq. (3.2), the following functions are defined, where q is an integer:

$$G_q(\mu) = \mu^q \sqrt{1-\mu^2} \left(\frac{19}{18} + \frac{11}{9}\mu^2 + \frac{2}{9}\mu^4\right) \tag{3.5}$$

$$F_q(\omega/T) = \frac{(\omega/T)^q}{1 + \exp(\omega/T)}. \tag{3.6}$$

In the previous equation, in writing $F(\omega/T)$, we are assuming that the structure function of the nuclear medium, in the notation of HR, $s(\omega/T)$, of the nuclear medium is unity, which is accurate

to first order[4]. An expansion to the next order, $(\omega/T)^2$, would likely shift the expected energy distribution of the differential flux to higher energies. Therefore, our assumption of $s(\omega/T) \simeq 1$ is in the direction of making the associated limits more conservative. Finally, the integral for the case of trapped KK gravitons, which make up the initial cloud bound to the NS, is given by:

$$N_{KK,n}(t=0) = 3\int_0^\infty d\omega \int_0^1 r^2\, dr \int_{1+U(r)}^1 d\mu\, \frac{\mathrm{d}^2 N_{KK,n}}{\mathrm{d}\omega \mathrm{d}\mu}. \tag{3.7}$$

In eq. (3.7), HR assume that the graviton creation is isotropic at the dimensionless radial distance from the neutron star center, r, scaled to the neutron star radius, R_{NS}. The integration over r is performed from the proto-neutron star's center to its surface, where $r = 1$, and the condition $\mu > 1 + U(r)$ selects the G_{KK} that are gravitationally trapped. As in HR, we model the neutron star's potential as Newtonian:

$$U(r) = -\frac{G_{\rm N} M_{\rm NS}}{R_{\rm NS} c^2} \times \begin{cases} \left(\frac{3}{2} - \frac{1}{2} r^2\right) & , \; r < 1 \\ \frac{1}{r} & , \; r \geq 1 \end{cases} \tag{3.8}$$

with $U_{NS} = -G_N M_{NS}/(R_{NS} c^2) = -0.159 (M_{NS}/1.4 M_\odot)(13\mathrm{km}/R_{NS})$.
The G_{KK} lifetime is [18][1]

$$\tau(m) = 1 \times 10^9 \mathrm{yr} \left(\frac{100\mathrm{MeV}}{m}\right)^3 \equiv \kappa^{-1} m^{-3}, \tag{3.9}$$

where $\kappa = 3.17 \times 10^{-23}\ \mathrm{MeV}^{-3}\mathrm{s}^{-1}$. Assuming an exponential decay of the KK gravitons, the number of KK gravitons remaining at time t after the core collapse is given by:

$$N_{KK,n}(t) = N_{KK,n}(t=0) \exp\left(-\frac{\mu t}{\tau(m)}\right) \tag{3.10}$$

Then, the time derivative (absolute value), of eq. (3.1), is given by:

$$\begin{aligned} \left|\frac{\mathrm{d}^2 \dot{N}_{KK,n}}{\mathrm{d}\mu \mathrm{d}\omega}\right| &= \kappa \frac{m^4}{\omega} N_{KK,n}(t) \\ &= Q_0 (RT)^n \Omega_n \Delta t_{NS} V_{NS} \kappa T^2 G_{n+3}(\mu) F_{n+2}(\omega/T) \exp\left(-\frac{\mu t}{\tau(m)}\right). \end{aligned} \tag{3.11}$$

3.2 Determining the Differential Flux by Monte Carlo Simulation

We determine the differential flux according to a Monte Carlo simulation that uses eq. (3.11). We calculate the mass distributions and the Lorentz parameters of the decaying gravitons. We then determine the momentum and energy distributions of the G_{KK}, considering the geometry of the decays. At the same time, the age of the NS determines the remaining number of gravitons. We also consider whether a given gamma ray can escape the NS magnetosphere. Finally, this determines the differential flux of gamma rays from the NS.

We carry out the Monte Carlo simulation of the differential flux in the following steps:

1) Sample ω from $F_{n+2}(\omega/T)$, as in eq. (3.11), for $0 < \omega/T < 20$ ($T = 30$ MeV). For $\omega/T > 20$, there is negligible contribution from the integral of $F_{n+2}(\omega/T)$.

2) Sample μ from $G_{n+3}(\mu)$, as in eq. (3.11), between $\mu_{\rm min}$ and $\mu_{\rm max}$. (Note that the sampling steps 1 & 2 are independent of each other, see HR.) To simplify the orbit calculation with only a small error, we assume that all of the created G_{KK} start their orbit at the center of the NS ($r = 0$)[2]. Thus we have $\mu_{\rm min} = 0.807$, corresponding to the G_{KK} escape velocity, and $\mu_{\rm max} = 0.926$, corresponding

[1] This takes into account competing decays to e^+e^- and $\nu\bar{\nu}$.
[2] We have calculated that this approximation is in the direction of making our limits more conservative.

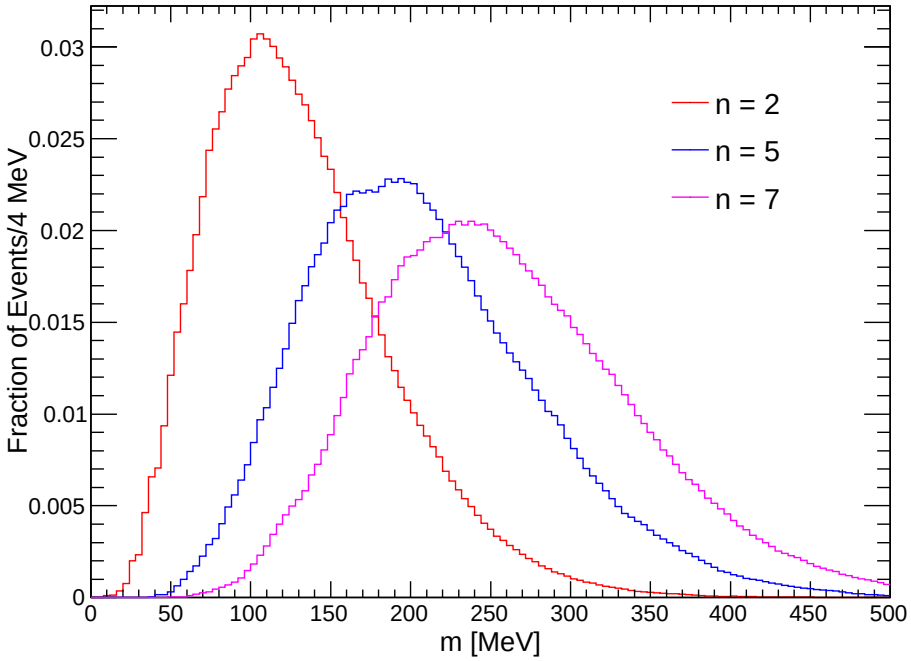

Figure 3: Unit-normalized distributions of KK graviton masses for $n = 2, 5, 7$, as determined according to Monte Carlo simulation.

to the minimum velocity to reach the neutron star surface, from $r = 0$. Having determined a value of μ, we determine the initial G_{KK} Lorentz factor $\gamma = 1/\mu$ and initial velocity $\beta = \sqrt{1-\mu^2}$. Given the geometry of the SN explosion, we assume, as do HR, that the G_{KK} orbits are radial. Using ω and μ, from steps 1 and 2, we determine a value for the mass, $m = \mu\omega$. Representative distributions of m, for different values of n, are shown in Figure 3.

Since we know the mass at this point, and given the age of the neutron star, $t_{\rm age}$, we calculate the exponential decay fraction, $F_{\rm decay} = \exp\left(-\frac{\mu t_{\rm age}}{\tau(m)}\right)$. We sample a real number u uniformly in the interval [0,1]: if $u > F_{\rm decay}$, then the event is rejected.

3) Sample the decay vertex r_0 for a given μ. The probability density function $P(r_0;\mu)$, which is shown in Figure 4 for two values of μ, is obtained as described in Appendix A. In Figure 5, unit-normalized radial profile of decay vertices as a function of radial coordinate, for n = 2, is plotted.

4) Sample the orbit direction isotropically ($-1 < \cos\theta < 1$, $-\pi < \phi < \pi$). This selects an orbit direction:

$$\hat{r}_0 = \sin\theta\cos\phi\ \hat{x} + \sin\theta\sin\phi\ \hat{y} + \cos\theta\ \hat{z} \tag{3.12}$$

where $\hat{x}, \hat{y}, \hat{z}$ are the unit coordinate directions in the NS frame. The $\hat{z}$ direction is chosen to align with the magnetic dipole axis of the NS. At the sampled decay vertex, r_0, we then obtain a velocity,

$$\beta' = R_{NS}\dot{r}/c, \tag{3.13}$$

where $\dot{r} = dr/dt|_{r=r_0}$ is obtained numerically, and the Lorentz factor,

$$\gamma' = 1/\sqrt{1-\beta'^{\,2}}. \tag{3.14}$$

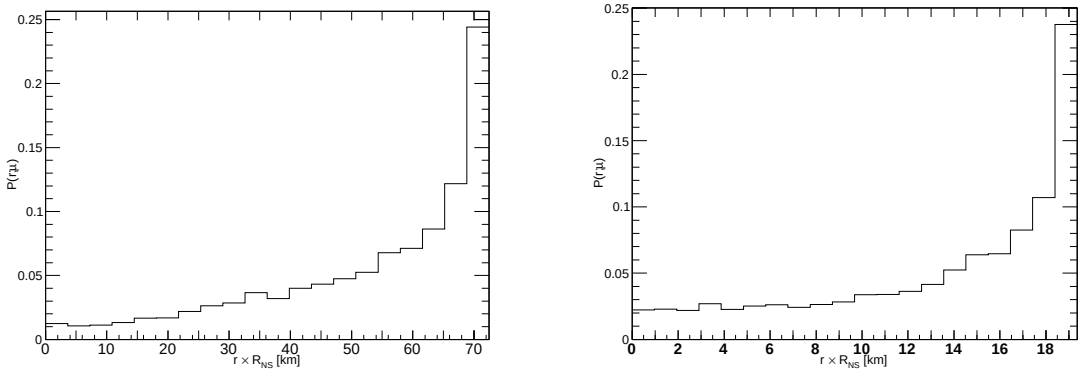

(a) $\mu = 0.83$ (b) $\mu = 0.90$

Figure 4: Radial probability density functions, $P(r;\mu)$, for 2 different values of μ. There are 20 linearly-spaced bins over the interval $[0, r_{\max} \times R_{NS}]$, and the $y-$axis is the fraction of events per bin.

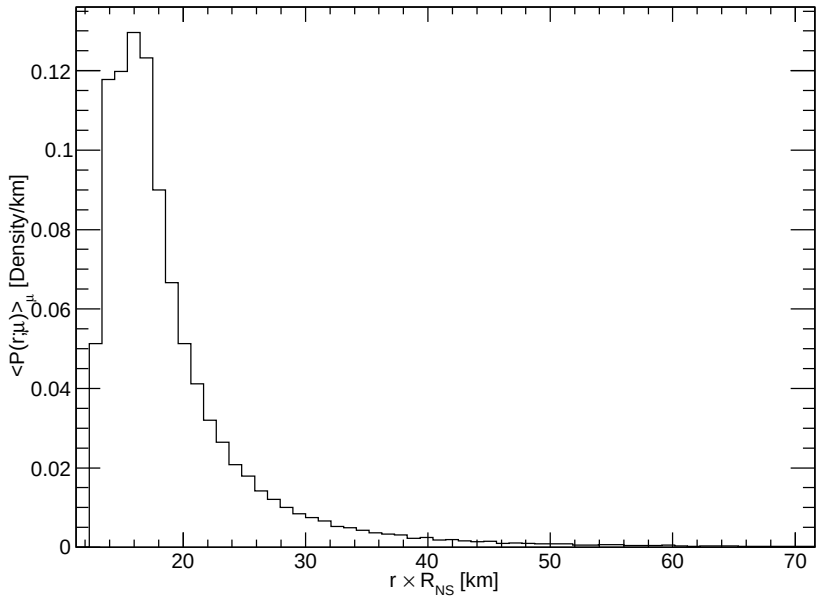

Figure 5: Unit-normalized radial distribution of decay vertices as a function of radial coordinate, $r_{\rm km}$, for $n = 2$. On the y-axis is plotted $\langle P(r;\mu)\rangle_{\mu}$, averaged over all μ between $\mu_{\min}$ and $\mu_{\max}$, for $1 < r < 5.5$.

Using the determined values of m and β', thus yields p^{ν}_{KK}, the G_{KK} 4-momentum in the NS frame at the decay vertex.

5) Determine the energy and momentum distribution of one of the two decay photons at decay point on the orbit with direction $\hat{r}_0$. We treat the other decay photon by multiplying the final flux by two. Full details of this procedure, as implemented in the Monte Carlo simulation, are given in Appendix B.

6) Determine whether the photon pair-produces in the neutron star magnetosphere: this probability

is given by $P_{\rm pp}(E_\gamma, \vec{r}, \vec{p}_\gamma)$. The probability for photon survival from pair production in the Monte Carlo simulation is then taken as $P_{\rm pp}(E_\gamma, \vec{r}, \vec{p}_\gamma) = \exp(-\tau_{pp})$. In Appendix C, we describe the computation of τ_{pp}. We sample a real number v uniformly on the interval [0,1]: if $v > P_{\rm pp}$, then the event is rejected.

3.3 The Final Flux Result from the Monte Carlo Simulation

The distribution defined by the Monte Carlo simulation, dN_n/dE_γ, is related to the differential flux by:

$$\frac{d\Phi}{dE_\gamma} = k_n R^n (d/\mathrm{kpc})^{-2} \frac{dN_n}{dE_\gamma}, \tag{3.15}$$

where the $n-$dependent constant k_n is given as:

$$k_n = \frac{1}{4\pi(3.086\times10^{21})^2} T^2 \kappa \left(\frac{T}{\hbar c}\right)^n \frac{2}{3} N_{0,n}\ \mathrm{cm}^{-2}\mathrm{s}^{-1}\mathrm{m}^{-n}. \tag{3.16}$$

and

$$N_{0,n} = N_{KK,n}(t=0)/(RT)^n, \tag{3.17}$$

where the factor κ is related to the decay rate as in eq. (3.9), and the factor $T/(\hbar c)$ is a conversion constant, which is numerically $1.52033\times10^{14}\ \mathrm{m}^{-1}$ at $T = 30$ MeV. Values of $N_{0,n}$ and k_n are tabulated in Table 3.

In the computation of dN_n/dE_γ, steps (3) and (7) of Section 3.2 reject events based on the decay from the lifetime and the pair production optical depth, respectively. In the case of a zero-age, zero-magnetic field neutron star source, the spectrum dN_n/dE_γ is normalized to 1. Formally, the distribution dN_n/dE_γ is defined by:

$$\frac{dN_n}{dE_\gamma} = \frac{1}{N_{ev}} \frac{dN'_n}{dE_\gamma} \tag{3.18}$$

where N_{ev} is the number of events in the Monte Carlo simulation. N_{rem}, the number of events remaining after the effects of decay and pair production are taken into account, is given by the integral:

$$N_{rem} = \int_0^{600\ \mathrm{MeV}} \frac{dN'_n}{dE_\gamma} dE_\gamma. \tag{3.19}$$

The upper limit of 600 MeV is determined by the condition $\omega/T \leq 20$[3]. The parameter η, defined as,

$$\eta \equiv \int_{100\ \mathrm{MeV}}^{400\ \mathrm{MeV}} \frac{dN_n}{dE_\gamma} \mathrm{d}E_\gamma \Big/ \int_{100\ \mathrm{MeV}}^{400\ \mathrm{MeV}} \frac{dN_n}{dE_\gamma}\Big|_{\mathrm{non-atten}} \mathrm{d}E_\gamma. \tag{3.20}$$

parameterizes the efficiency with which photons contribute to the spectrum, after signal attenuation effects of lifetime and pair production have been taken into account. Values for each source and n are shown in Table 4.

4 Limits on LED Results

4.1 Individual Limits

With all parameters for the ROI fixed, namely catalog sources and diffuse components, as determined in Section 2.3, upper limits on R^n are determined from spectral fitting based on the method of maximum likelihood. Fit values are determined by the MINUIT optimizer[19], and one-sided 95% confidence level upper limits are determined by performing a scan of the log-likelihood function in each ROI[19]. Statistical parameters of the fit are consistent with non-detection of the KK graviton

[3]The range of gamma-ray energies used to generate dN'_n/dE in the Monte Carlo is $0 < E_\gamma < 600$ MeV.

n	$N_{0,n}$	$k_n(\mathrm{cm}^{-2}\mathrm{s}^{-1}\mathrm{m}^{-n})$
2	6.47×10^{40}	7.126×10^{6}
3	3.46×10^{41}	5.799×10^{21}
4	1.94×10^{42}	4.963×10^{36}
5	7.40×10^{43}	4.511×10^{51}
6	7.05×10^{43}	4.355×10^{66}
7	4.97×10^{44}	4.452×10^{81}

Table 3: $n-$dependent constants, as defined in equations (3.17) and (3.16).

n	RX J1856−3754	J0108−1431	J0953+0755	J0630−2834	J1136+1551	J0826+2637
2	0.335	0.031	0.221	0.359	0.309	0.332
3	0.350	0.037	0.249	0.382	0.332	0.360
4	0.361	0.041	0.276	0.402	0.351	0.385
5	0.368	0.043	0.302	0.416	0.365	0.406
6	0.370	0.042	0.325	0.424	0.374	0.419
7	0.365	0.037	0.334	0.424	0.373	0.423

Table 4: Table of values of the attenuation parameter η, defined by eq. (3.20), for the different sources analyzed. These attenuation effects can be quite large. HR used only source RX J1856−3754 and J0953+0755. These values are calculated for 100 MeV$\leq E_\gamma \leq$ 400 MeV.

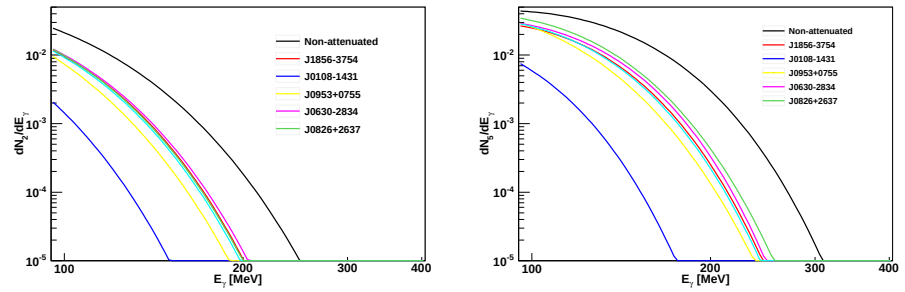

(a) $n = 2$ (b) $n = 5$

Figure 6: For $n = 2$ and $n = 5$, representative distributions of dN_n/dE_γ, according to eq. (3.18), for the non-attenuated spectrum and all neutron star sources considered, corrected for magnetic pair-production and age attenuation effects.

decay signal for all NS considered.As a check of this method, we compare upper limits obtained in this manner against upper limits computed using profile likelihood implemented by a different method in the Fermi-LAT *ScienceTools*, and find agreement within 10%. Additional systematic checks, due to uncertainties in the parameters of the background sources in the ROI, are also performed to verify the accuracy of the limits, for source RX J1856−3754 (the source with the best limits): the agreement in the flux upper limits is found to be 15% or better. The flux upper limits for each source and n are displayed in Table 5, and the corresponding limits on the LED size R are shown in Table 6.

4.2 Combined Limits

We use the following method to combine limits from multiple neutron star sources. A scan over the log-likelihood function in each ROI is done with respect to the parameter R^n, as shown in Figure 7. A curve of the change in log-likelihood, $|2\Delta \log \mathcal{L}|$, versus parameter value R^n, is generated for each source. Then the sum of these curves is taken for all the sources, and the parameter value

n	J1856−3754	J0108−1431	J0953+0755	J1136+1551	J0630−2834	J0826+2637
2	3.8	4.3	5.3	4.1	5.8	6.6
3	4.0	4.4	5.4	4.2	6.8	8.4
4	3.7	4.2	6.2	4.4	9.4	9.9
5	4.0	4.1	6.3	4.4	11	13
6	4.1	4.0	6.7	4.2	14	15
7	4.2	4.0	7.8	3.5	19	17

Table 5: Table of 95% C.L. flux upper limits (10^{-9} cm^{-2}s^{-1}) for the sources analyzed.

n	J1856−3754	J0108-14	J0953+0755	J1136+1551	J0630−2834	J0826+2637
2	9.5	49	22	23	24	29
3	3.9×10^{-2}	0.11	6.7×10^{-2}	6.9×10^{-2}	7.4×10^{-2}	8.4×10^{-2}
4	2.5×10^{-3}	5.4×10^{-3}	3.8×10^{-3}	3.9×10^{-3}	4.3×10^{-3}	4.8×10^{-3}
5	5.0×10^{-4}	9.1×10^{-4}	7.0×10^{-4}	7.1×10^{-4}	8.1×10^{-4}	8.6×10^{-4}
6	1.7×10^{-4}	2.8×10^{-4}	2.3×10^{-4}	2.3×10^{-4}	2.7×10^{-4}	2.8×10^{-4}
7	8.2×10^{-5}	1.3×10^{-4}	1.0×10^{-4}	1.0×10^{-4}	1.2×10^{-4}	1.3×10^{-4}

Table 6: Table of limits on extra dimensions size R (nm) for the sources analyzed.

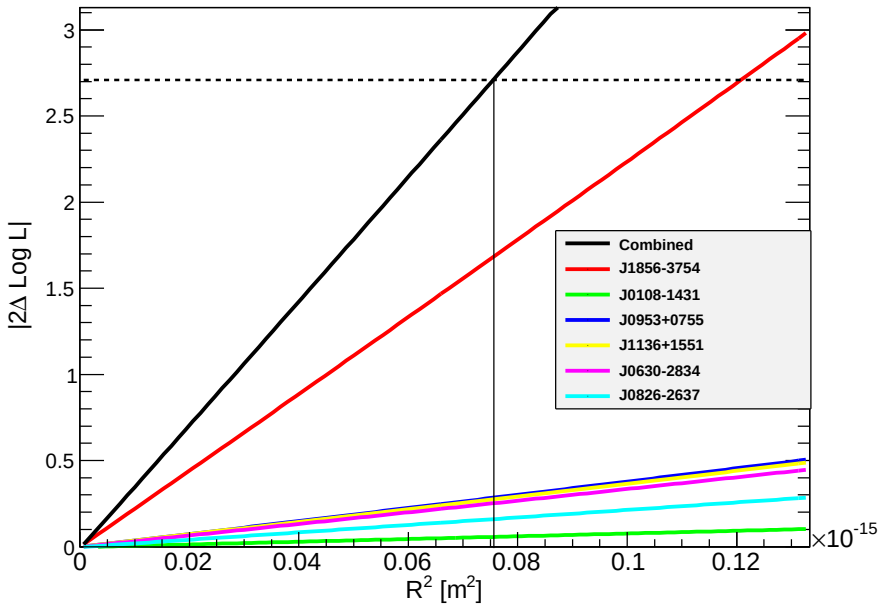

Figure 7: Plot of $|2\Delta \log \mathcal{L}|$ versus parameter value of R^n for $n = 2$. The 95% confidence level upper limit corresponds to a $y-$axis value of 2.71, shown by a dashed line. The sum of the curves, solid black, is used to obtain the posterior combined limit at the intersection with 2.71.

corresponding to intersection of that curve with a value of 2.71, corresponding to a one-sided 95% confidence level, is quoted as the combined limit value. The results of combining limits on R from this method, as well as results from HR, are presented in Table 7.

4.3 Dependence of LED Limits on Model Parameters

Dependence of the limits on model parameters, namely T, f_{KK}, and Δt_{NS}, have been evaluated. We have determined that the bounds on extra dimensions are quite sensitive to changes in T. Limits

n	R (nm) Combined	R (nm) HR
2	8.7	51
3	0.037	0.11
4	2.5×10^{-3}	5.5×10^{-3}
5	5.0×10^{-4}	9.1×10^{-4}
6	1.7×10^{-4}	2.8×10^{-4}
7	8.2×10^{-5}	1.2×10^{-4}

Table 7: 95% CL upper limits on R (nm) for each n, compared to HR2003 EGRET-based results[4].

n	$T = 30$ MeV	$T = 45$ MeV
2	9.5	1.2
3	3.9×10^{-2}	9.3×10^{-3}
4	2.5×10^{-3}	8.5×10^{-4}
5	5.0×10^{-4}	2.1×10^{-4}
6	1.7×10^{-4}	8.1×10^{-5}
7	8.2×10^{-5}	4.1×10^{-5}

Table 8: A comparison of upper limits on R (nm), evaluated for different values of T, for source RX J1856−3754.

n	$f_{KK}/10^{-3}$	R (nm)
2	6.3	9.5
3	8.7	0.035
4	7.4	2.5×10^{-3}
5	5.1	5.3×10^{-4}
6	9.1	1.7×10^{-4}
7	9.0	8.0×10^{-5}

Table 9: Table of f_{KK} values and combined upper limits on R (nm) for each value of n, assuming a Gaussian prior on f_{KK} (with mean 0.0075 and sigma 0.00144), as discussed in Sec. 4.4.

evaluated for source RX J1856−3754 for $T = 30$ MeV and a higher value $T = 45$ MeV, are compared in Table 8. The limits on LED are a strong function of temperature. The dependence enters through two effects: changing the constant k_n and changing the distribution of gamma-ray energies. The limits are affected, since $k_n \sim T^{-n-5.5}$; in other words, by modifying k_n, the bounds on LED size improve as:

$$R \sim \left(\frac{T}{30 \text{ MeV}}\right)^{-1-5.5/n}. \tag{4.1}$$

In addition, for higher temperatures, the distribution of energies is shifted to higher gamma-ray energies. Quantitatively, this increases the integral of the distribution function above 100 MeV, $\int_{100\text{MeV}}^{\infty} dN/dE\ dE$, which tends to improve the bounds. Limits placed on R from source RX J1856−3754 may vary by an order of magnitude, as shown in Table 8. We do not consider lower values of T, since according to [3], $T = 30$ MeV is a conservative lower limit on the SN core temperature.

By varying the timescale of core collapse, Δt_{NS}, the limits on R vary as $(\Delta t_{NS})^{-1/n}$. Estimates for this parameter vary from 5 s to 20 s[20], while we use the value of 7.5 s from HR. Thus, we see that the limits depend only weakly on variations of Δt_{NS} and f_{KK}.

n	Combined	CDF	DØ	LEP	ATLAS	CMS
2	230	2.09	1.40	1.60	1.5	3.2
3	16	1.94	1.15	1.20	1.1	3.3
4	2.5	1.62	1.04	0.94	1.8	3.4
5	0.67	1.46	0.98	0.77	2.0	3.4
6	0.25	1.36	0.94	0.66	2.0	3.4
7	0.11	1.29	-	-	-	-

Table 10: Comparison of 95% CL lower limits on M_D (TeV) with previous astrophysical limits and collider limits. *Combined* limits are obtained in this paper. Collider limits are taken from references [22–25]. ATLAS and CMS results are quoted where $\Lambda/M_D = 1$. ATLAS results are quoted with 3.1 pb^{-1} of data; CMS results are quoted with 36 pb^{-1} of data.

4.4 Effect of Uncertainties on f_{KK} on the Limits

Varying the fraction of energy lost into the graviton channel, f_{KK}, the limits on R vary as $f_{KK}^{-1/n}$. HR assumed $f_{KK} \simeq 0.01$, as consistent with diffuse gamma-ray measurements according to EGRET[16, 17]. However, a more accurate treatment from EGRET low energy diffuse measurements constrains f_{KK} such that $0.005 < f_{KK} < 0.01$. To take this range of values for f_{KK} into account when computing limits, we perform an analysis allowing for a Gaussian prior on the f_{KK} parameter, with a mean of 0.0075 and a sigma of 0.00144 (as obtained from the variance for a uniform PDF for f_{KK} between 0.005 and 0.01). We constrain this parameter to be the same across the 6 ROIs, for each value of n. This is possible within the framework of the Fermi-LAT *ScienceTools*; a similar technique was used to constrain dark matter signals from a combined analysis of Milky Way satellites with the Fermi-LAT[21]. Limits obtained in this manner are shown in Table 9.

5 Discussion and Conclusions

If M_D is at a TeV, then for $n < 4$, the results presented here imply that the compactification topology is more complicated than a torus, i.e., all LED having the same size. For flat LED of the same size, the lower limits on M_D results are consistent with $n \geq 4$. The constraints on LED based on neutron star gamma ray emission yield improvements over previously reported neutron star limits, based on gamma-ray measurements and combination of individual sources, as shown in Table 10. In addition, the results for the n-dimensional Planck mass are much better than collider limits from LEP and Tevatron for $n < 4$, and are comparable or slightly better for $n = 4$.

These limits may prove useful, especially for $n = 4$ case (where the limits are comparable to collider results), in the context of constraining phase space in searches for extra dimensions underway at the LHC. These results are also more stringent than those reported by short distance gravity experiments probing for deviations from the inverse square law. The most sensitive such experiment to KK graviton emission presented a result of 37 μm for $n = 2$ at 95% C.L.[26]; this is several orders of magnitude larger than the combined result reported here, of 8.7 nm.

Cassé *et al.* obtain upper limits significantly better than ours [27] (a factor ~ 20 for $n = 2$, though decreasing approximately as $1/n^2$ with increasing n), summing the contribution of all the expected NS in the Galactic bulge and comparing to the EGRET data. But it is should be noted that they do not account for age nor magnetic field attenuation, while the present analysis shows that both impact the photon distribution in a significant way. As these effects are not taken into account in HR, which the Cassé *et al.* paper is based on, their upper limits are necessarily underestimated. Furthermore, it should be emphasized that the 6 neutron stars analyzed here are chosen at high latitude to avoid the large systematic uncertainties involved in modeling the diffuse Galactic background. These are even larger in the low energy range that we are interested in here. An analysis of the bulge with the current Fermi-LAT instrument response functions and the current Fermi-LAT diffuse models could nominally improve the flux upper limits, but at the cost of a much less robust analysis, the systematics of which are difficult to evaluate. Within the Fermi-LAT collaboration, a better inner galaxy model is in

process, which is necessary before approaching a Galactic Bulge analysis. A Large Extra Dimensions analysis of the Galactic Bulge will be the subject of future studies.

A Appendix: Sampling Decay Vertices from Graviton Trajectories

In our model, due to the G_{KK} emission radially outward during the SN core collapse, the G_{KK} are not given any initial angular momentum; thus we assume that the G_{KK} oscillate on radial paths (completely eccentric orbits) through the center of the neutron star. In spherical coordinates (r, θ, ϕ), this is equivalent to the following constraints: $\dot{\theta} = \dot{\phi} = 0$. The orbital radial distribution, $P(r; \mu)$, is defined outside the neutron star by the radial Kepler equation, in which time is given as a function of the radial coordinate r[28][4]:

$$t(r) = t_k \left(\arcsin\left(\sqrt{kr}\right) - \sqrt{kr(1-kr)} + c_1 \right), \tag{A.1}$$

where:

$$k = r_{\max}^{-1} = \frac{1 + 1.5|U_{NS}| - \gamma}{|U_{NS}|} \ , \tag{A.2}$$

and:

$$t_k = \frac{R_{NS}}{\beta c k^2} \sqrt{\frac{k(1-k)}{1 - |U_{NS}|/\beta^2}}. \tag{A.3}$$

The solution inside the NS ($r < 1$) is defined as:

$$r(t) = \frac{\beta}{\sqrt{|U_{NS}|}} \sin(\Omega t) \ , \tag{A.4}$$

where the parameter $\Omega = \sqrt{|U_{NS}|}c/R_{NS} = 9.13 \times 10^3 \ \mathrm{s}^{-1}$.

Given that $t = 0$ is the time when the G_{KK} is created at $r = 0$, the radial distributions are determined by sampling time uniformly between the $t = 0$ and $t_{\max}$. $t_{\max}$ is given by the time to achieve the maximum distance, $r_{\max} = 1/k$, as in eq. (A.2). c_1 is determined from boundary conditions of position and velocity at the surface of the neutron star by solving the full equation of motion inside and outside the neutron star. The trajectories for a couple of values of β are plotted in Figure 8, while the radial distributions for representative values of μ, $P(r; \mu)$, are shown in Figure 4.

B Appendix: Relativistic Decay Kinematics of KK Gravitons

The energy is given by:

$$E_\gamma = \frac{1}{2}\gamma' m \left(1 + \beta' \cos\theta^*\right), \tag{B.1}$$

while the components of the photon momentum,

$$\vec{p'}_\gamma = p_{x',\gamma}\hat{x}' \ + \ p_{y',\gamma}\hat{y}' \ + \ p_{z',\gamma}\hat{z}', \tag{B.2}$$

in the neutron star frame relative to the direction of the G_{KK} are given by:

$$p_{x',\gamma} = \frac{1}{2} m \sin\theta^* \cos\phi^* \tag{B.3}$$

$$p_{y',\gamma} = \frac{1}{2} m \sin\theta^* \sin\phi^* \tag{B.4}$$

$$p_{z',\gamma} = \frac{1}{2}\gamma' m(\beta' + \cos\theta^*). \tag{B.5}$$

[4]The radial Kepler equation is not manifestly periodic. However, the full orbit cycle includes an interval over $0 < r < r_{\max}$, or a quarter of a cycle. Due to the symmetry of the orbit, our treatment of sampling the decay vertex from $t = 0$ to $t(r_{\max})$ is sufficient to obtain the full distribution of r_0.

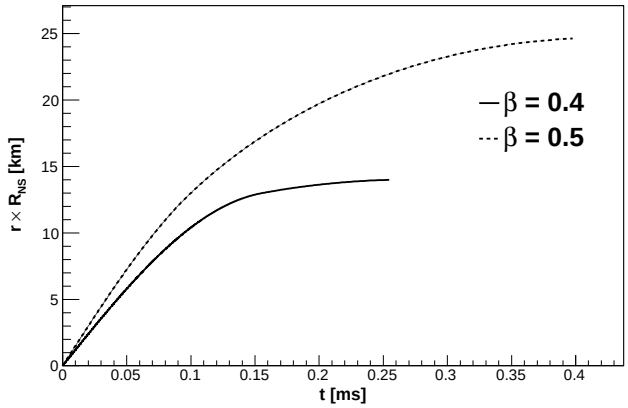

Figure 8: Trajectories for $\beta = 0.4$ and $\beta = 0.5$. Notice that for larger β, the KK graviton may achieve a farther maximum distance, $r_{\max} \times R_{NS}$. This figure shows one quarter of the orbit cycle.

The z' axis is defined by: $\hat{z}' = \hat{r}_0$. θ^* is the polar angle between the direction of the G_{KK} in the lab frame (z') and the decay photon in the rest frame of the G_{KK}, and ϕ^* is the angle in the $(x'-y')$plane. In this frame, $\hat{x}'$ is taken as perpendicular to $\hat{z}'$ in the $z - z'$ plane and in the direction of increasing θ, and $\hat{y}' = \hat{z}' \times \hat{x}'$. The coordinate systems used are depicted in Fig. 9. We sample a $\cos\theta^*$ value uniformly over the interval [-1,1], and ϕ^* uniformly over the interval $[-\pi, \pi]$, given isotropic emission of photons in the rest frame of the gravitons. Subsequently, we obtain momentum components of the gamma ray in the frame of the neutron star, $\vec{p}_\gamma$, by rotating back into the frame of the neutron star, using the direction of the momentum vector, $\vec{p}_{KK}$, as defined by step (5). This is needed for the next step.

C Appendix: Determining Photon Pair Production Optical Depths

Approximations for the pair-production attenuation are according to the treatment in Refs. [29, 30]. The attenuation coefficient depends on the parameter:

$$\chi(E_\gamma, \vec{p}_\gamma, \vec{r}) = \frac{E_\gamma}{m_e c^2} \frac{B_\perp(\vec{r}, \vec{p}_\gamma)}{B_{\rm cr}}, \tag{C.1}$$

where the critical field is given by

$$B_{\rm cr} = \frac{m_e^2 c^3}{e\hbar} = 4.414 \times 10^{13}\ {\rm G}, \tag{C.2}$$

$B_\perp$ is the magnetic field component of the neutron star perpendicular to the photon's momentum vector $\vec{p}_\gamma$, and E_γ is the photon energy. For the magnetic field of the neutron star, we assume a static dipole field,

$$\vec{B}(\vec{r}) = \frac{3(\vec{m}\cdot\hat{r})\hat{r} - \vec{m}}{r^3} \tag{C.3}$$

with dipole moment $\vec{m} = \frac{1}{2} B_{surf} R_{NS}^3 \hat{z}$. The attenuation coefficient, α, is given by:

$$\alpha(\chi(E_\gamma, \vec{p_\gamma}, \vec{r})) = \frac{\alpha_{\rm fs}}{\lambda\!\!\!^{-}_e} \frac{B_\perp(\vec{r}, \vec{p}_\gamma)}{B_{\rm cr}} \alpha_1(\chi), \tag{C.4}$$

where the reduced attenuation coefficient, $\alpha_1(\chi)$, is expressible as a function of χ in terms of a modified Bessel function of the second kind, with asymptotic limiting expressions for small and large values of χ (as plotted in Figure 10):

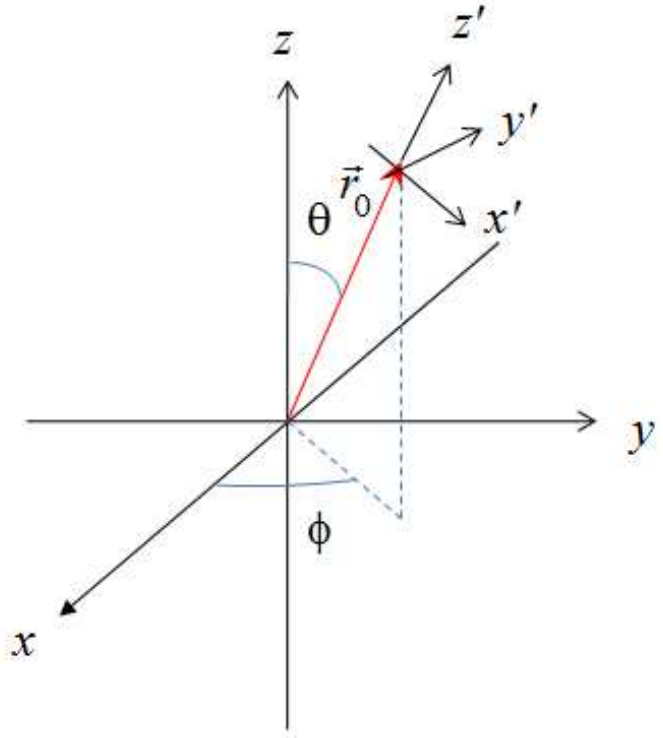

Figure 9: The coordinate system, as described in Appendix B.

$$\alpha_1(\chi) = 0.16\frac{1}{\chi}K_{1/3}^2\left(\frac{2}{3\chi}\right) = \begin{cases} 0.377e^{-\frac{4}{3\chi}}, \chi \leq 0.1 \\ \\ 0.597\chi^{-1/3}, \chi \geq 100 \end{cases} \tag{C.5}$$

In eq. (C.5), $\lambda\!\!\!^{-}_e = 3.861 \times 10^{-11}$ cm is the reduced electron Compton wavelength and $\alpha_{\rm fs}$ is the fine structure constant. The asymptotic expressions are used in the Monte Carlo simulation, where appropriate, in order to save computer time.

The optical depth τ_{pp} is calculated by path integrating the attenuation coefficient along the direction of the photon, from the point of decay, $\vec{r}_0 \equiv < x_0, y_0, z_0 >$, out to where $r_{km} = 7R_{NS}$ (where the field has attenuated to 0.3% of the surface field strength), according to

$$\begin{aligned} \tau_{pp} &= \int_{\rm path} \alpha \, {\rm d}s \\ &= \int_0^{s_{\rm max}} \alpha \left(\chi\left(E_\gamma, \vec{p}_\gamma, \vec{r}_0 + \hat{p}_\gamma s\right)\right) {\rm d}s \end{aligned} \tag{C.6}$$

In the preceding equation, $s_{\rm max}$, given by:

$$s_{\rm max} = -x_0p_1 - y_0p_2 - z_0p_3 + \sqrt{(x_0p_1 + y_0p_2 + z_0p_3)^2 + (7R_{NS})^2 - x_0^2 - y_0^2 - z_0^2}, \tag{C.7}$$

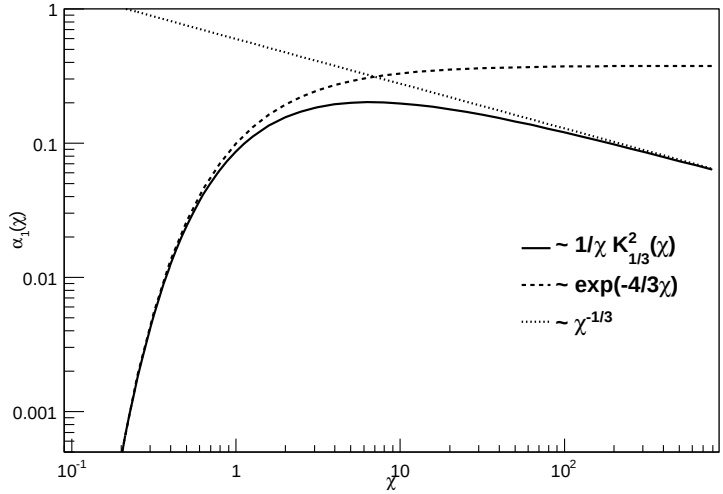

Figure 10: Plot of the reduced attenuation coefficient $\alpha_1(\chi)$ and limiting asymptotic expressions corresponding to eq. (C.5).

refers to the path length where the photon with direction unit vector *

$$\hat{p}_\gamma = \frac{\vec{p}_\gamma}{|\vec{p}_\gamma|} = p_1\hat{x} + p_2\hat{y} + p_3\hat{z} \tag{C.8}$$

is considered to have escaped the magnetosphere.

Acknowledgments

The *Fermi*-LAT Collaboration acknowledges generous ongoing support from a number of agencies and institutes that have supported both the development and the operation of the LAT as well as scientific data analysis. These include the National Aeronautics and Space Administration and the Department of Energy in the United States, the Commissariat à l'Energie Atomique and the Centre National de la Recherche Scientifique / Institut National de Physique Nucléaire et de Physique des Particules in France, the Agenzia Spaziale Italiana and the Istituto Nazionale di Fisica Nucleare in Italy, the Ministry of Education, Culture, Sports, Science and Technology (MEXT), High Energy Accelerator Research Organization (KEK) and Japan Aerospace Exploration Agency (JAXA) in Japan, and the K. A. Wallenberg Foundation, the Swedish Research Council and the Swedish National Space Board in Sweden.

Additional support for science analysis during the operations phase is gratefully acknowledged from the Istituto Nazionale di Astrofisica in Italy and the Centre National d'Études Spatiales in France.

References

[1] N. Arkani-Hamed, S. Dimopoulos, and G. Dvali, *The hierarchy problem and new dimensions at a millimeter*, *Phys. Lett.* **B429** (1998) 263, [hep-ph/9803315].

[2] C. Hanhart, D. R. Phillips, S. Reddy, and M. J. Savage, *Extra dimensions, sn1987a, and nucleon-nucleon scattering data*, nucl-th/0007016.

[3] G. G. Raffelt, *Stars as Laboratories for Fundamental Physics*. The University of Chicago Press, 1996.

[4] S. Hannestad and G. G. Raffelt, *Supernova and neutron-star limits on large extra dimensions reexamined*, *Phys. Rev. D* **67** (Jun, 2003) 125008, [hep-ph/0304029v2].

[5] ***Fermi*-LAT** Collaboration, W. Atwood *et. al.*, *The Large Area Telescope on the Fermi Gamma-Ray Space Telescope Mission*, *ApJ* **697** (June, 2009) 1071–1102, [arXiv:0902.1089].

[6] D. J. Thompson *et. al. Ap. J. Supplements* **86** (June, 1993) 629–656.

[7] A. Strong, I. Moskalenko, and O. Reimer *Ap. J.* **613** (2004) 962–976.

[8] A. Strong *Astron. and Astrophys. Supplement Series* **309** (2007) 35.

[9] http://fermi.gsfc.nasa.gov/ssc/data/analysis/software/aux/isotropic_iem_v02.txt.

[10] ***Fermi*-LAT** Collaboration, A. A. Abdo *et. al.*, *Fermi large area telescope first source catalog*, *Astrophysical Journal Supplement Series* **188** (2010), no. 2 405, [arXiv:1002.2280].

[11] ***Fermi*-LAT** Collaboration, R. Rando *et. al.* Proceedings of the 31st ICRC, July, 2009. astro-ph/0907.0626.

[12] R. Manchester, G. Hobbs, A. Teoh, and M. Hobbs, *The ATNF Pulsar Catalogue*, astro-ph/0412641.

[13] B. Berenji, *Search for Large Extra Dimensions Based on Observations of Neutron Stars with Fermi-LAT*. PhD thesis, Stanford University, 2011. http://purl.stanford.edu/sj534tb9150.

[14] http://fermi.gsfc.nasa.gov/ssc/data/analysis/documentation/Cicerone/.

[15] A. A. Abdo *et. al.*, *Fermi lat measurements of the diffuse gamma-ray emission at intermediate galactic latitudes*, *Phys. Rev. Lett.* **103** (2009) 251101, [astro-ph/0912.0973].

[16] P. Sreekumar *et. al. Ap. J.* **494** (1998).

[17] S. Hannestad and G. Raffelt, *New supernova limit on large extra dimensions*, *Phys. Rev. Lett.* **87** (2001) 051301, [hep-ph/0103201v2].

[18] T. Han, J. D. Lykken, and R.-J. Zhang, *On Kaluza-Klein states from large extra dimensions*, *Phys. Rev.* **D59** (1999) 105006, [hep-ph/9811350].

[19] F. James and M. Winkler, "Minuit user's guide." http://seal.web.cern.ch/seal/snapshot/work-packages/mathlibs/minuit/, June, 2004.

[20] S. Rosswog and M. Brüggen, *Introduction to High Energy Astrophysics*. Cambridge University Press, 2007.

[21] ***Fermi*-LAT** Collaboration, M. Ackermann *et. al.*, *Constraining dark matter models from a combined analysis of Milky Way satellites with the* Fermi*-Large Area Telescope*, *Phys. Rev. Lett.* **107** (2011) [arXiv:1111.0320].

[22] R. Franceschini, P. P. Giardino, G. F. Giudice, P. Lodone, and A. Strumia, *LHC Bounds on Large Extra Dimensions*, *JHEP* **05** (2011) 092, [hep-ph/1101.4919].

[23] http://lepexotica.web.cern.ch/LEPEXOTICA, 2004.

[24] V. Abazov *et. al.*, *Search for large extra spatial dimensions in the dielectron and diphoton channels in* $p\bar{p}$ *collisions at* $\sqrt{s}$ *=1.96 tev*, *Phys. Rev. Lett.* **102** (2009) 051601, [hep-ex/0809.2813v1].

[25] 16th International Workshop on Deep Inelastic Scattering and Related Subjects, *Searches for Large Extra Dimensions at the Tevatron*, July, 2008.

[26] D. Kapner *et. al.*, *Tests of the gravitational inverse-square law below the dark-energy length scale*, *Phys. Rev. Lett.* **98** (January, 2007) 021101.

[27] M. Cassé, J. Paul, G. Bertone, and G. Sigl, *Gamma rays from the galactic bulge and large extra dimensions*, *Phys. Rev. Lett.* **92** (Mar, 2004) 111102, [hep-ph/0309173].

[28] H. Goldstein, C. Poole, and J. Safko, *Classical Mechanics*. Addison Wesley, 3 ed., 2002.

[29] T. Erber, *High-energy electromagnetic conversion processes in intense magnetic fields*, *Rev. Mod. Phys.* **38** (1966) 626.

[30] V. Berestetskii, E. Lifshitz, and L. Pitaeveskii, *Quantum Electrodynamics* , vol. 4 of *Landau and Lifshitz Course of Theoretical Physics*. Pergamon Press, 2nd ed., 1982.